Field measurements, laboratory tests and empirical relations for investigating the solid-to-fluid transition of a rapid earthflow

(Article begins on next page)

24 July 2024

Dynamics of an active earthflow inferred from surface-wave monitoring

1

2   **Lara Bertello[1], Matteo Berti[1], Silvia Castellaro[2], Gabriela Squarzoni[1]**

3   [1] Department of Biological, Geological and Environmental Sciences, University of Bologna,

4   40127, Bologna, Italy

5   [2] Department of Physics and Astronomy, University of Bologna, 40127, Bologna, Italy

6

7   Corresponding author:

8   -   Matteo Berti matteo.berti@unibo.it

9   **Key Points:**

10   -   The earthflow material at our study site undergoes significant changes in shear stiffness
11   during rapid movements

12   -   Rayleigh velocity decreases as the earthflow accelerates, then gradually increases through
13   time as the landslide decelerates

14   -   Internal deformation clearly played an important role in the dynamics of the
15   Montevecchio earthflow

16
17

18   **Abstract**

19   Earthflows are clay-rich, slow-moving landslides subjected to periodic accelerations. During the
20   stage of rapid movement, most earthflows exhibit a change in behavior from a solid to a fluid-
21   like state. Although this behavior has been extensively documented in the field, the mechanism
22   leading to the rapid acceleration of earthflows is still poorly understood. Some studies suggest
23   that earthflows essentially behave as Coulomb plastic solids, attributing the flow-like appearance
24   to distributed internal shearing; others believe that these landslides can be treated as viscous
25   fluids, pointing out that the material undergoes a phase transition by increasing its moisture
26   content. Minimal data are currently available to support these different findings. In this study, we
27   present the results of periodic and continuous measurements of Rayleigh wave velocity carried
28   out in an active earthflow located in the Northern Apennines of Italy. Our data indicate that the
29   material undergoes significant changes in shear stiffness and undrained strength during rapid
30   movements. In particular, the material exhibits a substantial drop of Rayleigh wave velocity as
31   the earthflow accelerates, followed by a slow return to pre-disturbance Rayleigh velocities as the
32   landslide decelerates. Soon after a surge, the earthflow material is extremely soft and the
33   estimated gravimetric water content is above the liquid limit. In the following months, the shear
34   stiffness gradually increases and the water content decreases to the plastic limit following a non-
35   linear trend typical of a consolidation process. These data demonstrate that the earthflow
36   transforms into a viscous fluid by softening of the material and by water entrainment.

37

38   **1 Introduction**

39   Earthflows are among the most common type of landslides in many mountainous areas [*Keefer*
40   *and Johnson,* 1983*; Hungr et al.,* 2001*; Picarelli et al.,* 2005; *Simoni et al.*, 2013]. They occur in
41   fine-grained materials and are identified by a tongue or teardrop shape elongated in the
42   downslope direction [*Hutchinson,* 1988*; Cruden and Varnes,* 1996]. A specific feature of these
43   landslides is their complex style of movement [*Hutchinson,* 1970*; Bovis and Jones,* 1992].
44   Earthflows can continue to move slowly at a rate of less than 1 m per year over a long a period,
45   primarily by sliding on discrete basal and lateral slip surfaces [*Keefer and Johnson,* 1983*; Baum*
46   *et al.,* 2003*; Schulz et al.,* 2009]. Then, in response to critical rainfall conditions, they may
47   suddenly accelerate and attain high velocities (up to several m/h) for a limited time [*Varnes and*
48   *Savage,* 1996*; Coe et al.,* 2009]. During the surge of rapid movement, most earthflows create
49   geomorphic features like bulging toes, arcuate ridges, and streamlines that suggest a flow-like
50   behavior [*D'Elia et al,* 1998*; Giordan et al.,* 2013*; Handwerger et al.,* 2013].

51   Many researchers believe that the ability of earthflows to surge and rapidly accelerate is a
52   consequence of excess pore-water pressures generated along shear surfaces [*Keefer and Johnson,*
53   1983*; Baum et al.,* 2003*; van Asch and Malet*, 2009]. Others point out that such a behavior
54   indicates a sudden change in the mechanical properties of the material, like a loss of shear
55   stiffness or an increase of water content [*Picarelli et al.,* 2005*; Pastor et al.,* 2009*; Pastor et al.,*

56 2010; *Jongmans et al.,* 2015]. Although these factors are not mutually exclusive (an earthflow
57 could be triggered by an increase of pore-water pressures and subsequently undergo a change in
58 mechanical properties as the movement continues) their relative importance is still poorly
59 understood.

60 Pore-water pressure is certainly the most significant factor that can trigger the initial movement,
61 increase the displacement rate, or move earthflows on very gentle slopes [*Hutchinson and*
62 *Bhandari,* 1971; *Iverson and Major,* 1987; *Coe et al.,* 2009]. However, clay-rich soils do not
63 liquefy under an increase of pore water pressure [e.g. *Seed et al.,* 2003]. In soil mechanics, the
64 term "liquefaction" denotes a condition where a granular material behaves like a fluid because
65 the effective interparticle stress σ' (given by the difference between the total overburden stress
66 σ and the pore-water pressure u; *Terzaghi,* 1943) reduces essentially to zero causing the
67 particles to lose contact with each other. Soil liquefaction occurs in loosely packed, cohesionless
68 soils (mostly sand) that tend to decrease in volume when subjected to shear stress [*Seed et al.,*
69 2003]. Clay materials with measurable plasticity are not susceptible to liquefaction because they
70 have undrained cohesion, thus the shear strength of clays does not become zero when the
71 effective stress becomes zero [*Seed et al.,* 2003; *Robertson,* 2010]. Accordingly, most
72 researchers consider earthflows as Coulomb plastic solids that primarily move by sliding, and
73 attribute the flow-like appearance to distributed internal shearing rather than mass liquefaction
74 [*Keefer and Johnson* 1983; *Baum et al.,* 2003; *Hungr et al.,* 2001].

75 Nevertheless, fine-grained materials can change from solid to plastic to fluid as the water content
76 increases, showing distinct changes in behavior and consistency. The Atterberg limits are a
77 conventional measure of the critical water contents at which these changes occur [*Casagrande,*
78 1932]. The transition from a plastic to a fluid state due to an increase of the water content is
79 referred to hereafter as "fluidization". Fluidization differs from liquefaction because the material
80 undergoes a change in behavior with a change in volume, while liquefaction essentially assumes
81 undrained conditions and constant void ratio. Field observations indicate that earthflows may
82 exhibit a significant increase in water content during mobilization [*Prior et al.,* 1968;
83 *Hutchinson et al.,* 1974]. Most active earthflows are so soft that they do not support a person's
84 weight [*Keefer and Johnson* 1983], or become "so wet and mascerated that all the debris may
85 truly flow by continuous internal deformation" [*Craig* 1979 cited in *Moore* 1988, p. 59]. Fluid
86 rheologists have extensively investigated the solid-fluid transition of clays in laboratory
87 rheometrical tests, defining the existence of a yield stress that separates a rigid/elastic domain
88 and a fluid domain [*Coussot et al.,* 1998; *Ancey,* 2007; *Mainsant et al.,* 2012b]. Most of these
89 experiments are conducted on clay slurries at or above the liquid limit (LL), which is the
90 moisture content at which soil changes from a plastic to a fluid state measured using the
91 conventional Casagrande apparatus [*Casagrande,* 1932].

92 The reasons for this different behavior (shear sliding of a plastic solid vs viscous flow of a liquid
93 material) are still unclear, but more can be learned by collecting relevant data from rapidly
94 moving earthflows. The monitoring technique recently proposed by *Mainsant et al.* [2012a] can

95   be useful for this purpose. The method relies on the continuous measurement of Rayleigh wave

96   velocity (V_R) as an indicator of material fluidization (or loss of stiffness). Rayleigh waves are

97   elastic waves which travel near the ground surface with a combination of longitudinal

98   compression and dilation [*Richart et al.,* 1970]. These waves are the principal component of

99   ground roll and propagate about 10% slower than shear waves [*Telford et al.,* 1990]. The idea

100   behind the method is that, as the shear wave velocity in a fluid tends to zero [*Reynolds,* 1997],

101   the Rayleigh wave velocity measured inside a landslide should strongly decrease if the solid

102   material fluidizes [*Mainsant et al.,* 2012a*, Mainsant et al.,* 2015]. *Mainsant et al.* [2012a]

103   monitored an earthflow located in the Swiss Alps and observed that Rayleigh velocities

104   decreased continuously and rapidly for several days before a catastrophic stage of movement,

105   suggesting a dramatic change in the mechanical properties of the material. To our knowledge,

106   this is the only study that has documented the process of solid-to-fluid transition in earthflows.

107   Therefore, more field data need to be collected in different geological and morphological settings

108   in order to understand if rapid surging of earthflows is accompanied by softening and fluidization

109   of the material, or mainly occurs by shearing along internal and boundary shear surfaces.

110   In this study, we used Rayleigh wave velocity to investigate the behavior of the Montevecchio

111   landslide, an active earthflow located in the Northern Apennines of Italy (Savio River valley,

112   Province of Cesena). In February 2014, the earthflow entered a period of intense activity that

113   lasted for 17 months until June 2015. During this period, the earthflow experienced three surges

114   of rapid movement characterized by the fluidization of the moving mass. We documented this

115   process by periodic and continuous measurements of Rayleigh wave velocities carried out using

116   the active Multichannel Analysis of Surface Waves (MASW) [*Park et al.,* 1999] and the passive

117   Refraction Microtremors (ReMi) techniques [*Louie,* 2001]. Geophysical data were integrated by

118   continuous measurements of rainfall and landslide displacement. The data reveal a complex

119   relationship between rainfall, displacement rate, and Rayleigh velocity, providing new insight

120   into the dynamics of active earthflows.

121

2 Study Area

123   The Montevecchio landslide is located in the Northern Apennines of Italy, approximately 16 km

124   to the south of the city of Cesena. The landslide occupies the valley of the Ribianco Creek, a

125   tributary of the Savio River (Figure 1). The area is characterized by relative gentle slopes

126   (inclination in the range of 7° to 17°) covered by grass and native brush, and ranges in elevation

127   from 70 to 215 m a.s.l.. The upper part of the basin has typical badland morphologies

128   characterized by small gullies, steep slopes (35° to 45°) and low vegetation coverage.

129   Bedrock geology consists of shallow marine deposits belonging to the Colombacci Formation

130   [*Ricci Lucchi et al.,* 2002]. This Formation was deposited from the Late Miocene to the

131   Holocene with a maximum thickness of 450 meters. In the study area, the Colombacci Formation

132   consists of predominant marly and silty clay interbedded with thin layers of fine sandstone

133   (sandstone/clay ratio is lower than 1/3). The clay is stiff to very stiff with a dark grey-blue color
134   when fresh, and becomes soft and brown when weathered. The sandstone layers are loose or only
135   weakly cemented, the color turning from grey to yellow with weathering. The Colombacci
136   Formation is well exposed on the source areas of the earthflow (zone A-B-C; Figure 1).

137   Old landslide deposits originated by multiple earthflow events occupy about 45% percent of the
138   Ribianco basin (Figure 1). These deposits consist of a clay-rich colluvium containing scattered
139   blocks of weakly cemented sandstone of variable size. The slopes covered by landslide deposits
140   have an average inclination of about 13°. These landslides are subjected to periodic reactivations.
141   The term reactivation (or remobilization) is current to indicate a phase of high activity after a
142   long period of dormancy [*Cruden and Varnes,* 1996]. Herein, reactivation is used to indicate a
143   stage of rapid movement (with a velocity of several meters per day or per hour) that leads to the
144   complete mobilization of the earthflow material. In the last 50 years, the Montevecchio landslide
145   reactivated once in 1979, when it almost reached the houses and the road at the toe, then in 1997,
146   1999, 2002, 2005, 2006, and 2008 with local movements in the upper part of the slope. During
147   the last period of activity (February 2014 to June 2015) the earthflow underwent a new complete
148   remobilization (see next section).

149   Results from geotechnical tests show that the earthflow material is fairly uniform. It has medium
150   plasticity (Liquid Limit=50%; Plastic Index=26%) and it is composed on average by 15% sand,
151   45% silt, and 40% clay. Blue methylene tests provide a specific surface of the clay of 112±1
152   m^2/g, which is a typical value for an illite [*Hang et al.,* 1970] and an activity index of the clay
153   fraction [Acb; *Lautrin,* 1989] equal to 12.5±0.5. The density is 1850 kg/m^3 in saturated
154   conditions and 1500 kg/m^3 for the dry soil (average values of 500 g undisturbed samples taken
155   within one meter of the surface). Direct shear tests give a critical state friction angle ϕ'_{cs}=20° and

156   a residual friction angle ϕ'_r=13°.The local climate is Mediterranean with two main rainy periods
157   from autumn to early winter (October to December) and during spring (March to May). The
158   average annual precipitation is 780 mm and the average annual snowfall is about 30 cm. The
159   average annual temperature is 14°C and it ranges between 17° and 29° during the dry season and
160   between 1° and 20° C during the wet season.

161

162   **3 Recent activity of the Montevecchio landslide**

163   In February 2014, after a prolonged rainfall of 109 mm in 16 days, the Montevecchio earthflow
164   entered into a new period of activity. The trigger rainfall was above the probabilistic rainfall
165   threshold established for the area [*Berti et al.,* 2012] and caused a large number of landslides in
166   all the Emilia Romagna Region. The activity lasted for 17 months (until June 2015) and within
167   this period the earthflow underwent three major reactivations (1st reactivation: February 1, 2014;
168   2nd reactivation: February 25, 2015; 3rd reactivation: May 25, 2015). As mentioned above, the
169   term "reactivation" indicates the complete remobilization of the existing landslide deposits from

170   the source area to the toe. Hereafter we also use the term "partial reactivation" to indicate the
171   remobilization of only a portion of the landslide (generally the upper part) and "suspended
172   phase" to indicate the time after a reactivation when the landslide slows down [*Schadler,* 2010].
173   A reactivation corresponds to a stage of rapid earthflow movement with downslope velocity on
174   the order of meters per hour. This stage generally lasts 2-5 days, then the velocity gradually
175   decreases with time approaching some nonzero value. In fact, during the 17 months of activity,
176   the landslide never stopped and the minimum-recorded velocity was on the order of few
177   mm/day.

178   The first reactivation (February 1, 2014) started as sliding failure in the source area A (Figure 2a)
179   and caused a retrogression of the headscarp of about 8 m. The landslide quickly propagated
180   downslope (Figure 2b) at a speed of several meters per hour, and in a couple of days reached the
181   toe (Figure 2c-d). Local authorities decided to protect the houses and the road by removing the
182   advancing toe material, which was continuously excavated for weeks and deposited on the
183   fluvial terrace to the other side of the road. In March and April 2014, the earthflow partially
184   reactivated several times after heavy rain. The excavations at the toe continued and four earth
185   berms were built across the landslide to stop the movement (Figure 1). From May 2014, the
186   earthflow entered a suspended phase that lasted about 9 months. During this period, the landslide
187   velocity decreased gradually from m/day to cm/day, with episodes of acceleration of 10-20 cm in
188   a few days after intense rainfall events. The suspend phase ended with the second reactivation of
189   February 25, 2015. This time the initial sliding failures involved both the source area A and B
190   (Figure 1) causing further retrogression of the headscarps, the complete mobilization of the
191   earthflow, and the destruction of two earth berms. Further movements occurred in March 2015,
192   then the landslide slowed down and almost stopped at the end of April 2015. The third and last
193   reactivation was in May 25, 2015. Again, the landslide remobilized into a fluid, fast-moving
194   earthflow that quickly reached the toe. Here local authorities removed the material 24 hours a
195   day to save the houses. In June 2015, the earthflow almost stopped and significant consolidation
196   works were carried out. Five earth berms were built across the landslide (Figure 1) and a trench
197   drain system was realized to stabilize the middle-upper part of the slope. The landslide remained
198   essentially stable in the following years with some localized slides in the source area and along
199   the north flank.

200

201   Field observations provide qualitative but valuable information on the reactivation mechanism of
202   the Montevecchio earthflow. In all the three cases, the mobilization starts with a relatively small
203   translational slide in the source area (zones A-B-C; Figure 1) that occur during or shortly after
204   rainstorms. In the source area the bedding planes dip with the same direction as the slope scarp at
205   an angle of 40° with the horizontal, promoting slope instability by translational sliding and
206   flexural buckling. The rock exposed on the scarp is an alternation of marly clay and fine
207   sandstone, with estimated values of the uniaxial compressive strength in the range 1-5 MPa
208   (measured in the field by simple index tests; *Hoek and Brown,* 1977). Although the rock is fresh

209 or only slightly weathered, it completely disintegrates after rupture and turns into loose, fine-
210 grained debris. The material detached from the scarp accumulates on the head of the gently
211 inclined earthflow deposits causing ground bulging, cracks openings, and the formation of lateral
212 shear surfaces. *Hutchinson and Bhandari* [1971] first introduced the term undrained loading to
213 describe the failure of a saturated landslide deposit due to undrained compression and
214 consequent rise of pore-water pressures.

215 After the initial slide, a surge of rapid movement can occur leading to the transformation of the
216 earth slide into an earthflow. Evidence for this change in behavior includes: i) the landslide
217 suddenly accelerates from millimeter-centimeters/day to meters/hour; ii) a variety of flow
218 structures appear on the ground surface, such as arcuate pressure ridges parallel to the contour
219 lines, hummocks, lateral levees, and tongue-shaped lobes; iii) the material softens by increasing
220 the water content. This latter evidence is of particular interest. After each surge we surveyed the
221 landslide and perform several simple tests to assess material softness by inserting a steel tube (5
222 cm diameter, 2 m long) into the ground. These qualitative data confirm that soon after a
223 reactivation the earthflow is in a fluid state, at least within the upper 2 m. The material shows the
224 consistency of a clay slurry, and we could easily insert the steel tube into the ground by hand
225 throughout its length. Unfortunately, the depth of the fluidized layer remains unknown because
226 the earthflow was not accessible to heavy machinery after a surge.

227 After the stage of rapid movement, the earthflow decelerates. The velocity at the toe and along
228 the main track gradually decreases from m/day to cm/day, and the landslide continues to move
229 within lateral shears zones with minor internal deformation. Interestingly, the material in the
230 shear bands (20 to 40 cm thick) remain very soft for several weeks after the surge, while the
231 landslide body becomes apparently stiffer and stronger.

232

233 **4 Field data**

234 **4.1 In situ measurements of Rayleigh wave velocity**

235 <u>Methodology</u>

236 We documented the reactivation of the Montevecchio earthflow by means of periodic and
237 continuous measurements of Rayleigh wave velocities, carried out using two standard
238 techniques: the active Multichannel Analysis of Surface Waves (MASW) [*Park et al.,* 1999] and
239 the passive Refraction Microtremors (ReMi) techniques [*Louie,* 2001]. Both techniques exploit
240 the properties of Rayleigh waves of different wavelengths to excite the material at different
241 depths, thus travelling at different velocity: short wavelengths normally propagate slower (due to
242 the lower velocity of shallow layers) while long wavelengths, which excite deeper layers,
243 propagate faster [*Aki e Richards,* 1980*, Ben-Menahem and Singh,* 1981]. MASW focuses on the
244 signal produced by artificial sources while ReMi exploits signals from natural sources.

245   The velocity of Rayleigh waves of different wavelengths into the ground is derived from the
246   seismic signal recorded at different positions (a minimum of two) over time. Different
247   mathematical algorithms can be used for this derivation. One of the simplest is to filter the signal
248   at different frequencies and cross-correlate the filtered signal among all the geophone couples to
249   find the time lag. Since the distance between each geophone couple is known, the propagation
250   velocity can be obtained by dividing this distance by the time-lag. The result of the cross-
251   correlation algorithm (normalized to the auto-correlation function) can be plotted in frequency-
252   velocity plots as shown in the conceptual example of Figure 3.

253   Since the dispersion of surface waves is a multimodal phenomenon, different velocity values are
254   possible at the same frequency, each one corresponding to a different propagation mode. In the
255   case of an ideal source, ideal receiver geometry, and ideal material (homogeneous and isotropic
256   half-space), the fundamental mode is dominant in terms of energy. However, in real cases this
257   does not always happen. Selecting the dispersion curve of the fundamental mode or correctly
258   sorting the higher modes implies a degree of subjectivity which represents one of the limits of
259   the method as extensively discussed in the literature [*Gucunski and Woods,* 1992*; Tokimatsu et*
260   *al.,* 1992*; Foti et al.,* 2014*; Castellaro,* 2016]. Here, we restrict the discussion to what can be
261   inferred from Figure 3. The propagation velocity distribution of a surface wave at a specific
262   frequency is given by the normalized cross-correlation function at that frequency. The graduated
263   colour bar in Figure 3 represents the probability density distribution (in linear scale from 0 to 1)
264   of the normalized cross-correlation function. The maxima of the distribution (blue dots in Figure
265   3) are the velocities associated with each frequency. The narrower the peaks (red shaded areas),
266   the better the degree of accuracy of the velocity determination. The point A in Figure 3 indicates
267   the Rayleigh velocity for a frequency of 30 Hz and the associated error bar, defined as the
268   velocity range with a probability value higher than 0.8.

269   Rayleigh waves induce the maximum displacement in the subsoil at a depth which is
270   approximately $z = \left| \dfrac{\lambda}{3}, \dfrac{\lambda}{2} \right|$, where λ is their wavelength and the range depends on the Poisson's
271   ratio [*Jones*, 1962]. This approximate relation provides a way to determine both the velocity
272   profile in the subsoil (remembering that $\lambda = V_R / f$, where the velocity V_R and the frequency f
273   are those of Figure 3) and the maximum investigation depth. Refined inversion algorithms are
274   available to evaluate the velocity profile with depth based on specific modeling of Rayleigh
275   wave propagation in multilayered media exist, but are beyond the goal of this paper. Here we
276   refer to the common approximation of converting wavelength to depth by using the relation
277   $z = \lambda / 2.5$ [*Foti et al.*, 2014; *Castellaro*, 2016]. From this relation it also follows that the ideal
278   aperture of the array is at least half the desired investigation depth $z_{max} / 2$ [*Rix and Leipski*,
279   1991; *Park et al.*, 2007], although arrays with $z_{max} / 4$ can still be effective under specific
280   circumstances [*Castellaro*, 2016].

281   These standard techniques differ from the method used by *Mainsant et al.* [2012a] in a major
282   aspect. *Mainsant et al.* [2012a] derived the velocity values in the subsoil from the cross-
283   correlation of the signal between two geophones at known distance. The two geophones are
284   planted in the stable ground on both sides of the landslide and provide the average Rayleigh
285   velocity across the investigated section. Since the geophones are located outside the landslide,
286   the system can operate even when the earthflow is rapidly moving. This is an important
287   advantage compared to standard techniques that instead require access to the landslide area.
288   However, the use of two geophones is appropriate only when the signal propagation is aligned
289   with the geophone line. If this is not the case, the method provides apparent velocity values,
290   larger than the real values by a factor $1/\cos\alpha$ where α is the angle between the signal
291   propagation direction and the geophone alignment. The method can still provide correct results
292   (that is an apparent velocity distribution centred on the real velocity value) provided that the
293   noise distribution around the geophone line is homogeneous [*Mulargia and Castellaro*, 2013].
294   To overcome this limitation we decided to use standard methods by employing: a) active sources
295   in line with the array, thus ensuring observation of real velocity values, b) a larger number of
296   geophones, which allows one to compute more precise (statistically redundant) velocity values
297   with depth, and c) in the case of purely passive surveys, where the source position with respect to
298   the array is unknown, we examined several dispersion curves and retained in the analysis only
299   those showing the lowest velocity values, which are by definition those closer to the real velocity
300   values (given that $V_{apparent} = V_{real}/\cos\alpha$). Moreover, standard techniques provide measurements

301   of Rayleigh velocity that allow comparing the state of the material in different locations along
302   the landslide.

303

304   <u>Periodic surveys</u>

305   At Montevecchio, periodic measurements were done every 1-2 months (Tab. 1) along seven
306   seismic lines. Four lines were located within the landslide area and three just outside the
307   landslide as shown in Figure 4.

308

309   *Table 1: Periodic seismic surveys carried out at Montevecchio (location of the measurement*
310   *sections in Figure 4).*

Date	Measurement section						
	A	B	C	D	E	F	G
2014/05/07	X	X	X	X	X	X	X
2014/06/06	X	X	X	X	X	X	X
2014/06/06	X	X	X	X	X	X	X
2014/07/27	X	X	X	X	X	X	X
2014/08/28		X	X	X			
2015/01/23		X	X	X			
2015/02/18			X				
2015/03/11		X	X	X			
2015/03/24		X	X	X			
2015/04/17		X	X	X			

Date							
2015/04/24	X	X	X	X			
2015/04/30			X		X	X	X
2015/05/07	X	X	X	X			
2015/05/19	X	X	X	X	X	X	X
2015/06/08	X	X	X	X			
2015/06/19		X	X	X			
2015/07/09	X	X	X	X			
2015/07/16		X	X				
2015/08/05	X	X	X	X			
2015/08/27			X				
2015/09/04	X	X	X	X			

311

312 We used six vertically polarized 4.5 Hz geophones, pressed firmly into the ground and set at
313 intervals of 2 m each (total length of the seismic lines 10 m). A 10 m aperture antenna can detect
314 waves as long as 40 m, which corresponds to maximum investigation depth of ~12. The first 5
315 minutes of each acquisition were done in the passive mode (ReMi), just acquiring the ambient
316 seismic noise, while the last minute was in the active mode (MASW) by putting a seismic source
317 (a jump of the operator) about 5 m apart from the first geophone, in order to ensure as planar as
318 possible wavefronts at the geophones. All the geophones were connected to a Soilspy Rosina
319 acquisition system and data were processed using the software Grilla (http://MoHo.world).

320 The data were analyzed to obtain the fundamental dispersion curves. Besides the problems
321 generally related to the interpretation of dispersion curves (see above) the difficult field
322 conditions provided further sources of uncertainty. During the dry season, the surface of the
323 landslide was pervaded by desiccation cracks and open fractures (Figure 5a-b) and a firm
324 coupling of the geophones with the ground was difficult. Conversely, during the rainy season or
325 after the major reactivation events (Figure 5c) the material was fluid and most measuring points
326 were not accessible. Both the variable ground conditions and the different location of the
327 measuring points affected the accuracy of the results.

328　Figure 6 shows a typical Rayleigh-wave phase-velocity vs. frequency plot (spectrum) obtained at
329　Montevecchio using active (Figure 6a) and passive (Figure 6b) methods. The dispersion curve
330　can be traced by following the red-shaded areas of the frequency-velocity plots. In the active
331　mode (Figure 6a) the dispersion curve is generally well defined over a wide range of frequencies
332　and fundamental mode can easily be identified. In the passive mode (Figure 6b) the curve is
333　discontinuous and the fundamental mode can be recognized only in some frequency intervals.
334　For example, the dispersion curve shown in Figure 6b is not well defined around 10 Hz, from 13
335　to 17 Hz and above 25 Hz. In fact, active source methods are generally capable of resolving
336　higher frequencies than passive methods because the source and receiver array can be tailored to
337　the desired frequency range. On the contrary, the source for the ReMi survey was ambient
338　seismic noise that typically contains significant low frequency energy and lacks high frequency
339　signal, which can lead to poor resolution of shallow soil layers [*Louie*, 2001; *Cox and Wood*,
340　2010; *Strobbia and Cassiani*, 2011].

341

342　<u>Continuous measurements</u>

343　Periodic surveys were integrated by continuous measurements of surface wave velocity. To this
344　aim, a cost-effective self-produced monitoring system was designed to include these features: 1)
345　easy to install in the field and quick to remove; 2) low maintenance; 3) light enough to be carried
346　by hand; 4) resistant to harsh field conditions (intense rainfall events, large ground
347　displacements); 5) minimal energy consumption; 6) compatibility with other geotechnical
348　sensors. A number of preliminary tests were conducted to find the optimal configuration.
349　Different combinations of sampling rate (50 to 300 Hz), number of geophones (2 to 4) and
350　duration of the acquisition session (from 30 s to 5 min) were tested in order to balance the
351　desired signal accuracy with the capabilities of the datalogger and the power requirement. This
352　appeared to be a suitable configuration for our needs: i) Campbell CR1000 data logger with
353　CFM100 Compact Flash Module (2GB); ii) 4 vertical geophones at 4.5Hz with 4 signal
354　amplifiers (gain=500); iii) power supplied by a 12 V 7 Ah battery recharged by a 20 W solar
355　panel. Good results were obtained by reading the four geophones at 300 Hz for 2 minutes every 1
356　hour, thus simulating the execution of 24 ReMi surveys every day.

357　The monitoring system was installed at Montevecchio in May 16, 2014. The geophones were
358　placed on the main track of the earthflow channel with a spacing of 2 m (Figure 4, blue line) and
359　buried at a depth of 20 cm (Figure 7a-b) to avoid the atmospheric thermal effect and to ensure an
360　adequate coupling with the ground [*Beekman,* 2008]. In the periodic surveys burial was not
361　required because we hand-tamped around the geophones to ensure good coupling. The signals
362　acquired with this type of approach require to be stable in time, implying a relatively constant
363　background noise over the period of interest [*Hadziioannou et al.,* 2009]. Based on direct
364　observation during the first field tests, the main source of ambient seismic noise vibration was
365　the national road located at the toe of the landslide (about 400 m away from the monitoring
366　system) which constitutes a spatially stable background noise. The data collected from the

367 datalogger were periodically downloaded and analyzed using the same software adopted for
368 periodic surveys (Grilla).
369 Also in this case, dispersion curves were sometimes difficult to interpret, thus we decided to
370 classify each curve as "good", "fair", or "bad" according to quality of the phase velocity
371 spectrum (Figure 8). Figure 8a shows a dispersion curve classified as "good": here the
372 fundamental as well as a number of higher modes can clearly be distinguished in a wide
373 frequency interval (5-50 Hz). The case (b) shows a "fair" dispersion curve in which the
374 fundamental mode can be recognized only at low frequencies (5-10 Hz). Case c) shows a
375 dispersion curve classified as "bad" because the fundamental mode cannot be detected. Bad
376 curves are generally due to electrical problems with the signal amplifiers, cable ruptures, or bad
377 ground coupling. For the purpose of the analysis, we only considered the "good" (a) or "fair" (b)
378 dispersion curves. As representative velocity values, we picked the central points of the red range
379 (which represents the highest probability range of velocity), while we used the red range
380 boundaries (probability value higher than 0.8) to define the error bars (Figure 3).

381 Field monitoring was difficult and sometimes risky due to the strong landslide activity. Figure
382 7c-d shows the monitoring system just after the reactivation of February 25, 2015: all the
383 equipment was moved downslope for about 100 m, the rain gage was destroyed and both the
384 geophones and the amplifiers were lost. The landslide was not accessible for almost two months,
385 not even to retrieve the equipment. The system was rebuilt and reinstalled on May 7, 2015. Less
386 than one month later, the earthflow reactivated again and the monitoring system was again
387 destroyed. During the monitoring period, we reinstalled the system six times because of the
388 continuous landslide movements.

389

4.2 Landslide displacement

391 Landslide movement was measured using continuous GPS monitoring and a time-lapse camera.
392 The GPS system consists of one reference station located in a stable area outside the landslide
393 and three rover stations installed along the earthflow (Figure 4). Rover GPS devices were
394 LEICA-GMX901 antenna (single frequency; 10 Hz update; horizontal accuracy: 3 mm + 0.5
395 ppm; vertical accuracy: 5 mm + 0.5 ppm) powered by two batteries (12 V 14 Ah in parallel) and
396 recharged by a 60 W solar panel. Rover stations were equipped with Wi-Fi direction antennas
397 (model Ubiquiti Nanostation M5) for transmitting data to the reference station. Both the GPS
398 receiver, the control unit, and the WiFi antenna were installed on a 2 m long pole equipped with
399 a helicoid tip that was screwed into the ground. The reference station was a dual-frequency
400 LEICA GMX902 antenna connected to an industrial PC. The PC run the software Leica GNSS
401 Spider used to process the data in real time. Power to the reference station was provided via a
402 connection to the grid at 220 V. Raw data are processed in real time to determine the GPS
403 coordinates of rovers in differential mode with respect to the reference station, i.e by calculating
404 the baseline, which is the distance between rover and reference GPS antennas. Since the baseline

405 of rover 1 (the one closest to the monitoring station) is nearly coincident with the direction of
406 movement of the landslide, the measured displacements were not projected.

407 The time-lapse camera is a Brinno TLC200 that was placed outside the right flank of the
408 earthflow (Figure 4) shooting the monitoring system. The camera has a focal length of 36 mm
409 and it was set to take one picture every 30 minutes with a resolution of 640x480 pixels. An AVI
410 video is created in the camera during recording, which results in a file of about 0.2 MB/frame
411 stored on a 8 GB SD card. The analysis of these videos was carried out with the free software
412 Tracker. The displacement was calculated knowing the dimension of an object in the camera
413 view (a wood pole with red/white markings) and its distance from the camera. The pole was
414 placed in the midline of the channel in order to measure the maximum velocity of the earthflow.

415

416 **5 Results**

417 **5.1 Periodic acquisitions**

418 Periodic seismic surveys were performed at Montevecchio from May 2014 to September 2015.
419 For sake of clarity, we divide the dataset into the three periods that followed the three main
420 reactivations.

421 Figure 9 illustrates the data collected after the first reactivation (May 2014-January 2015). The
422 charts show the profiles of Rayleigh wave velocity (V_r) measured inside (section A, B, C, D)
423 and outside (section E, F) the landslide area in the different campaigns (location in Figure 3).
424 The dates of the seismic surveys are reported as days elapsed since the last mobilization (in this
425 case the partial reactivation of April 27, 2014) in order to highlight the variation of V_r with time.
426 As it can be seen, the Rayleigh wave velocity increased over time inside the landslide, while it
427 remained constant outside. In particular, soon after the reactivation (10 days later) the landslide
428 material was characterized by very low values of $V_r \approx 50$ m/s with no significant differences
429 between the four sections. Then V_r increased. The rate of recovery along the earthflow was
430 however different: in the source area (section A) it was faster than in the lower part (section D),
431 whereas sections B and C showed intermediate values. For instance, in 271 days, the Rayleigh
432 wave velocity at a depth of 5 m increased by 100, 45, 30, and 15 m/s moving from section A to
433 D.

434 The data collected after the second reactivation (March to May 2015) provided similar results
435 (Figure 10). The first survey was done only 14 days after the reactivation of February 25, when
436 the landslide material was still partially fluid. The data show very low velocity profiles
437 throughout the earthflow (see sections B, C, D; section A is missing because it was not
438 accessible) revealing a sharp drop in V_r compared to initial conditions (end of the period in
439 Figure 9). V_r remained low in the next two weeks due to the continuous movements of the
440 earthflow, then gradually increased to the values shown before the mobilization. In this case, the

441 recovery rate was similar in the three sections. The Rayleigh wave velocity outside the landslide
442 remained constant and equal to that measured in the first period ($V_r \approx 200\text{-}250$ m/s).

443 The data of the third period (June to September 2015) show a similar trend (Figure 11). Again,
444 the lowest values of V_r occurred soon after the reactivation of May 25, 2015, then the wave
445 velocity increased to the initial value. During this third period the variation of V_r with time was
446 quite complex (especially in sections B and C) because of the extensive consolidation works
447 carried out from July to September 2015, that triggered partial reactivations of the earthflow
448 around the construction area of the earth berms. The last survey was on September 4, 2015. After
449 that, local authorities installed a dense network of trench drains and drainage channels to
450 stabilize the landslide and most of the material was reworked up to a depth of 2-4 m.

451 The chart in Figure 12 summarizes the data collected inside and outside the landslide area over
452 the whole period. For this comparison, we used the Rayleigh wave velocity measured at a depth
453 of 2 m, where the dispersion curves are well defined. Despite the difficulties posed by the harsh
454 field conditions and the uncertainties in these geophysical measurements, a clear trend emerges
455 from the data: the Rayleigh wave velocity dropped to very low values as the earthflow
456 reactivated, then it increased to the initial values following a non-linear trend.

457

458 5.2 Continuous monitoring

459 Continuous monitoring was designed to capture the change in material properties during the
460 mobilization of the earthflow. The Montevecchio monitoring system was installed in May 2014
461 (after the first reactivation of February 12014) and recorded the second and third reactivation.
462 The third reactivation of May 25, 2015 is the best documented being both the GPS and the time-
463 lapse camera active. Figure 13 shows the data collected three weeks before and after this event.
464 The red and blue dots indicate the Rayleigh wave velocity at a frequency of 11 and 15 Hz, which
465 correspond to an approximate depth of 1 and 2 m respectively. The gray dots are the velocities at
466 8 Hz (approx. 3 m). The investigation depth is restricted to the first meters because the dispersion
467 curves obtained by the monitoring system are poorly represented for low frequencies (section
468 4.1). However, since the velocity profiles obtained by the periodic surveys are almost linear with
469 depth and vary evenly over time (Figure 11), we believe that these data are representative of the
470 general behavior of the landslide.

471 In the first three weeks of May 2015, the landslide was slowly moving at a rate of less than 1
472 cm/day. Rayleigh velocities were fluctuating around 50-55 m/s, as typically observed during the
473 suspended state of activity of the landslide. On May 22, it started to rain at 01:10 AM and
474 continued until May 24 08:40 AM with 47 mm in 56 hours. About 11 hours after the beginning
475 of the rain (small inset in Figure 13a) the landslide started to accelerate and the displacement rate
476 increased by five times (from 0.8 cm/day to 4 cm/day, Figure 13b). The Rayleigh velocity
477 dropped to 30-35 m/s (30% drop) and remained low for the next two days May 23 and 24, until

478   the first surge of rapid movement (Figure 13c). The first surge started around midnight on May
479   24, 16 hours after the end of the rain: the landslide quickly accelerated to 5.8 m/day and reached
480   the peak velocity of 10 m/day (200 times higher than the day before) in the morning of the 25. In
481   a few hours the earthflow moved downslope of 5-7 m disrupting the geophones array. The
482   landslide then slowed down and the velocity decreased to 1.2 m/day in the following 10 hours. A
483   second rainfall event of 24 mm in 3 hours occurred on May 26 05:30 PM, leading to the
484   complete reactivation of the earthflow. This second surge lasted three days with a peak velocity
485   of 22 m/day and a total displacement of about 35 m. The geophones were buried by the landslide
486   and most of the equipment was destroyed.

487   The monitoring system was reinstalled on June 3, 2015. The data collected after the surges
488   confirm the results of periodic surveys, showing an increase of Rayleigh velocities as the
489   landslide decelerates. Three weeks after the reactivation, V_r almost returned to the initial values
490   of 50-60 m/s. Rayleigh velocities remained essentially constant until the end of July 2015
491   (Figure 14). On July 26, the local authorities started to build an earth dam in the source area A
492   (location in Figure 1) causing a partial reactivation of the landslide. The monitoring system
493   recorded an increase of the displacement rate (from about 5 cm/day to 40 cm/day) accompanied
494   by a decrease in V_r of about 20% (Figure 14c). Again, V_r increased to 50-60 m/s as the
495   earthflows decelerates.

496   Figure 15 shows the data collected during the second reactivation of February 25, 2015. The
497   general trend depicts a progressive increase of the displacement rate (Figure 15a-b) accompanied
498   by a decrease of the Rayleigh velocity (Figure 15c). However, a closer look shows some
499   complexity. Rayleigh velocity started to decrease below its normal range on January 31, while
500   the landslide was slowly moving at a constant speed of about 5 cm/day. Time lapse videos
501   revealed that in those days the ground started to bulge due to the rapid loading of an upload slide.
502   In the next days the Rayleigh velocity remained low (around 45 m/s) and essentially constant,
503   although the displacement rate increased in response to the rainfall event of February 3-6 (160
504   mm in 4 days). The lowest values of Rayleigh velocity (less than 40 m/s) were recorded anyway
505   just before the complete reactivation of February 25.

506   Figure 16 shows the data recorded five months after the first surge, during a long stage of
507   suspended activity (July to November 2014). In that period, the landslide was moving very
508   slowly (Figure 16a) with a trend of slightly decreasing velocity(few mm/day, Figure 16b). As
509   expected, the Rayleigh velocities remained essentially constant with small fluctuations around 50
510   m/s (Figure 16c). The temporary accelerations exhibited by the landslide in response to the
511   rainfall events did not cause any detectable decrease of Rayleigh velocity.

512

513 **6 Discussion**

514 The data collected at Montevecchio indicate that the mechanical properties of the earthflow
515 material change during surges. The periodic measurements of Rayleigh wave velocity (Figure 9-
516 11) provide the clearest evidence of this variation. Soon after a surge, the values of V_r are very
517 low within the entire thickness of the flowing mass, then they gradually increase through time as
518 the landslide decelerates. The general trend is similar for the three reactivations and across the
519 landslide (Figure 12), although the absolute values of V_r and the rate of recovery are quite
520 different. Possible reasons for these differences are the variable thickness of the landslide, the
521 influence of partial reactivations, the different rate of residual movement, and the effect of
522 consolidation works. For instance, the construction of an earth berm close to section A (Figure 1)
523 is the reason for the rapid increase of V_r observed in that area after the first reactivation (Figure
524 9A), while the continuous excavations carried out at the toe of the landslide explain the low rate
525 of recovery in section D (Figure 9D).

526 Figure 17a provides an overall view of the data collected by periodic surveys. Each point shows
527 the mean Rayleigh velocity measured at a depth of 2 m inside (sections A to D) and outside
528 (sections E and F) the landslide area. Time is reported as number of days elapsed since the last
529 surge. The chart shows that inside the earthflow the Rayleigh velocity increases with time of 30-
530 40% following a power function. A strong increase of V_r occurs in the first 50-70 days after a
531 reactivation, then the velocity seems to attain a constant value (though the curve is not well
532 constrained in the long term). Outside the landslide area, V_r is constant and remarkably higher.
533 These data can be interpreted according to the general theory of surface wave propagation.
534 Rayleigh waves travel with a horizontal wave speed V_r slightly lower than the shear wave speed
535 V_s. The ratio V_r/V_s is a function of the material's Poisson ratio v [*Achenbach*, 2012]:

536

537
$$\frac{V_r}{V_s} = \frac{0.862 + 1.14v}{1+v} \qquad (1)$$

538

539 varying from 0.90 for $v = 0.5$ (soft soils in undrained conditions) to 0.95 for $v = 0.2$ (stiff soils
540 in drained conditions). In an elastic solid, the velocity of a shear wave is controlled by the solid's
541 density (ρ) and shear modulus (G_0):

542

543
$$V_s = \sqrt{\frac{G_0}{\rho}} \qquad (2)$$

544

545   where the notation G_0 indicates the initial shear modulus at very small strains (0.001% or less).

546   Since the density ρ has a negligible effect on V_s compared to G_0, the observed variation of

547   Rayleigh velocity at Montevecchio can be interpreted as a change in the shear stiffness of the

548   earthflow material. Figure 17b shows the values of G_0 computed from the shear velocity

549   assuming $\nu = 0.5$ and constant soil density $\rho = 1600$ kg/m^3 (taken as the average between the

550   density at the liquid limit $\rho \approx 1400$ kg/m^3 and the average density measured in the field $\rho \approx$

551   1800 kg/m^3). As can be seen, the shear modulus of the earthflow material is very low soon after

552   mobilization ($G_0 \approx 5$ MPa) then increases up to 15-20 MPa in a few months. This change in

553   shear stiffness suggests a transition from a very soft to a stiff clay [*Ortiz et al.*, 1986].

554   Similar results are obtained using undrained shear strength (s_u). A number of V_s-based

555   correlations have been proposed in the literature to estimate s_u. *Mayne* [2007] derived a

556   generalized relation between shear wave velocity and cone tip resistance (q_t in kPa) suitable for

557   clay materials from soft to firm:

558

559     $V_s = 1.75 q_t^{0.627}$ (3)

560

561   *Nguyen et al.* [2014] found a correlation between G_0 and net cone tip resistance ($q_t - \sigma_{v0}$, where

562   σ_{v0} is the total vertical stress) better constrained for soft clays:

563

564     $G_0 = 89.1 (q_t - \sigma_{v0})^{1.50}$ (4)

565

566   These relationships can be inverted to obtain q_t and combined with the classical formula

567     $s_u = (q_t - \sigma_{v0}) / N_{kt}$ (where $N_{kt} \approx 14$ is a bearing factor; *Robertson*, 2009) to get an estimate of

568   undrained strength. The results obtained with the two formulas (using V_s from 64 to 109 m/s in

569   equation (3), and G_0 from 7 to 19 MPa in equation (4)) are similar: the undrained strength is as

570   low as 10-20 kPa soon after reactivation and increases up to 30-50 kPa in a few months. Two

571   cone penetration tests carried out at the toe of the earthflow three weeks after the first

572   reactivation confirm these estimates: in the first 8 m, the tests show a uniform profile of s_u with

573   depth with average values in the range 15-20 kPa. According to the British Standard 5930 [*BSI*,

574   2015], this change in strength indicates the transition from a very soft to a firm clay.

575   The data collected by the monitoring system provide evidence of changes in the material
576   properties before a surge. Rayleigh velocity decreases about 20-30 m/s (about 30% of the initial
577   value) just before the rapid movements of February and May 2015 (Figure 13-15), indicating that
578   the material softened as the earthflow approached a new reactivation. The observed drop is about
579   10 times larger than the standard deviation of measurements computed when the landslide is not
580   moving (2.2 m/s obtained as the average of the standard deviations calculated for the three
581   frequencies in Figure 16). However, the relationship between displacement rate and Rayleigh
582   velocity is not simple. In particular, there is no correlation between landslide speed and V_r drop
583   (apparently, V_r decreases a similar amount regardless of the velocity attained by the landslide)
584   and also the timing of the drop may differ (section 5.2). Unfortunately, available data do not
585   allow one to establish why there are these differences, mostly because of the limited accuracy of
586   the measurements. A series of tests conducted in the field showed that the dispersion curve
587   obtained without an active seismic source, and using only 4 geophones instead of the 6 used in
588   periodic surveys, is often discontinuous or poorly defined. This makes it difficult to detect the
589   Rayleigh velocity of the fundamental mode and introduces significant uncertainties in the data.

590   Despite these uncertainties, the data seem to provide a consistent picture: the earthflow material
591   softens during a surge, and then recovers to the initial state when the velocity decreases and the
592   landslide comes to rest. The observed behavior cannot be explained by a simple sliding
593   mechanism in which the landslide moves as a plastic solid. The drop in shear stiffness clearly
594   plays an important role in the rapid movement of the Montevecchio earthflow.

595   What is now more difficult to establish is whether the measured variation of V_r may indicate a
596   solid-to-fluid transition of the earthflow. In principle, we could infer the void ratio e of the
597   material from the shear stiffness G_0, and compute the gravimetric water content at saturation w
598   ($w = e / G_s$, where $G_s \approx 2.7$ is the specific gravity of solids) in order to evaluate the state of the
599   earthflow. However, going from Rayleigh velocities to void ratio is fraught with uncertainties,
600   mostly because the various forms of the $G_0 - e$ functions published in the literature might not
601   apply to our field conditions. In particular, the measured change of Rayleigh velocity at
602   Montevecchio could be due to the opening (or closing) of fissures and cracks within the
603   earthflow rather than dilation (or contraction) of the soil skeleton. The following analysis
604   therefore provides only a rough estimate of e and should be taken with care.

605   *Santos and Correia* [2000] compared a number of empirical $e - G_0$ relationships and proposed
606   the following function for soils with high percentages of fines:

607

608      $$G_0 = 4000 e^{-1.3} p^{0.5} \tag{5}$$

609

610   where p is the mean effective stress. Inverting the equation and assuming $p \approx \sigma'_{v0} = 12$ kPa

611   (effective vertical stress at a depth of 2 m considering $\rho = 1600$ kg/m^3 and water table at the

612   ground surface) we can estimate e from G_0. According to equation (5) the observed increase of

613   shear stiffness after a surge (G_0 from 5 to 20 MPa) corresponds to a decrease of void ratio from

614   $e \approx 2$ to $e \approx 0.7$. The equivalent change in terms of gravimetric water content is from $w \approx 80\%$

615   to $w \approx 30\%$. By comparing these values with the Atterberg limits (plastic limit $PL = 26\%$; liquid

616   limit $LL = 50\%$) it turns out that the water content of the earthflow material is well above the

617   liquid limit soon after a surge and close to the plastic limit a few months later. These results are

618   consistent with the field evidence of a fluidized surface of the earthflow that becomes stiffer with

619   time (section 3).

620   The change of void ratio with time is of particular interest because it allows a quantitative

621   analysis of observed behavior. Figure 18 shows this trend using a normalized void ratio index ($\hat{e}$

622   ) that depicts the relative variation of e with respect to the minimum and maximum values

623   estimated above ($e_{min} = 0.7$ and $e_{max} = 2$):

624

625   $$\hat{e} = \frac{e_{max} - e}{e_{max} - e_{min}} \tag{6}$$

626

627   The trend of the experimental points is consistent with the exponential decrease of pore volume

628   (and increase of material stiffness) that occurs with time during the consolidation of a porous

629   material. In fact, it agrees well with the theoretical trend (red curves in Figure 18) predicted by

630   the one-dimensional consolidation theory [*Terzaghi,* 1943]. Terzaghi's consolidation theory

631   allows one to compute the change in void ratio of the soil skeleton to the change in effective

632   stress by means of a coefficient of consolidation (c_v) determined in the oedometer test. The

633   theoretical curves in Figure 18 are computed using typical values of c_v for fine-grained material

634   [*Holtz and Kovacs*, 1981]. These simple calculations suggest that the Montevecchio earthflow is

635   in a fluid state soon after a rapid stage of movement and returns to a plastic state as the material

636   consolidates.

637   A further point of discussion is the possible use of this technique for early- warning of earthflow

638   movement. *Mainsant et al.* [2012a] detected a decrease of the relative Rayleigh wave velocity

639   well before the reactivation of their monitored landslide (a first 2% drop about one month before

640   the movement, and a second 7% drop four days before). *Mainsant et al.* [2015] carried out some

641   laboratory experiments on artificial clay slopes having different water content and confirmed a

642   drop in V_r values before the failure. Based on these the authors suggested that field monitoring of

643   surface wave velocity could be potentially used to predict landslides [*Mainsant et al.,* 2012a].

644   These results are more uncertain. Also in our case the Rayleigh velocities start to drop a few days

645   before a surge (Figure 13 and 15) but the relationship between V_r and landslide speed is not

646   straightforward. Besides the uncertainty in the data (as discussed above), a possible explanation

647   is that we started to monitor the landslide after a major reactivation (February 2014) that

648   completely remobilized the existing deposits, generating a dense network of pervasive cracks

649   and fissures within the landslide mass. The two surges of February and May 2015 were

650   subsequent reactivations of a completely remolded material. In these conditions, the effect of

651   pre-failure cracking and deformations is probably negligible, and we could only detect the main

652   changes in shear stiffness associated with the very rapid movements. Therefore our data cannot

653   prove (or disprove) the use of Rayleigh wave monitoring for early landslide detection.

654

655   Finally, we comment on the technique adopted at Montevecchio for the continuous monitoring of

656   Rayleigh wave velocity. The system configuration (4 vertical geophones at 4.5 Hz; 2 min

657   sessions at 300 Hz every 1 hour; passive mode) proved its effectiveness, but with a low accuracy

658   compared to periodic surveys. Several modifications can be done to improve results: 1) combine

659   active and passive mode acquisition in order to improve the dispersion curve at high frequency

660   ranges (for example, using an automatic hammer controlled by the datalogger that hits the

661   ground during the measurement session); 2) use more geophones to ensure an adequate data

662   redundancy [*Tokimatsu,* 1997]. As an alternative to surface wave monitoring, one could use a

663   down-hole probe specifically designed for long-term monitoring in order to get direct

664   measurements of shear wave velocity inside an active landslide. A further improvement is to

665   combine geophysical data with geotechnical sensors to monitor the water content of the material.

666   Conventional dieletric sensors have an accuracy of 2-3% [*Starr and Paltineanu,* 2002] and

667   should easily detect the dramatic change of water content required for the earthflow to transition

668   to a liquid state.

669

670   **7 Conclusions**

671   Rayleigh wave monitoring proved to be an effective method to investigate changes in material

672   properties that occur in active earthflows. In this study, we monitored rainfall, ground

673   displacement, and Rayleigh wave velocity of an earthflow located in the Northern Apennines of

674   Italy during a two-year period of intense activity. Based on these data, several conclusions can be

675   drawn:

676   1. As the earthflow accelerates approaching a stage of rapid movement, the material exhibits a

677   significant drop of Rayleigh wave velocity (V_r); V_r then gradually increases through time as the

678   landslide decelerates, returning to the initial values in a few months.

679   2. The observed variation of Rayleigh velocity indicates that the earthflow material undergoes a
680   significant change in shear stiffness and undrained strength during each reactivation.

681   4. A simple mechanism of rigid-block sliding cannot account for the observed changes of
682   material properties; therefore, internal disturbance and remolding play an important role in the
683   dynamics of the Montevecchio earthflow.

684   5. Tentative estimates of the gravimetric water content suggest that the earthflow material is well
685   above the liquid limit soon after a surge and decreases with time to the plastic limit following a
686   non-linear trend typical of a consolidation process; these estimates are consistent with the field
687   evidence of a fluidized surface of the earthflow that becomes stiffer with time.

688   6. At Montevecchio, there is no clear evidence that Rayleigh velocity starts to decrease well
689   before the landslide starts to move, as found by *Mainsant et al.* [2015]. However, in our case the
690   material was completely remolded by previous movements, thus we probably missed the initial
691   cracking that occurs when the landslide reactivates after a long period of dormancy.

692   7. Because of the difficult field conditions and limited accuracy of the data, available
693   measurements do not allow the precise identification of the relationship between rainfall,
694   displacement rate, and Rayleigh velocity. In order to get better results from field monitoring we
695   suggest the use of 6-8 geophones (instead of 4), the use of an active seismic source controlled by
696   the data logger, and installation of soil moisture sensors at different depths for direct
697   measurement of water content inside the landslide.

698

707

References

709   Achenbach, J.D. (2012). *Wave propagation in elastic solids*. Amsterdam, The Netherlands:
710   Elsevier.

711   Aki, K., & Richards, P. G. (1980). *Quantitative seismology, Theory and Methods*. San Francisco:
712   W. H. Freeman & Co. DOI10.1017/S0016756800034439

713   Ancey, C. (2007). Plasticity and geophysical flows: A review. *Journal of Non-Newtonian Fluid
714   Mechanics, 142*(3), 4-35.

715 Baum, R.L., Savage, W.Z., & Wasowski, J. (2003). *Mechanics of Earth Flows*. Paper presented
716 at International Workshop on Occurrence and Mechanisms of Flows in Natural Slopes and
717 Earthfills, Sorrento, Italy.

718 Beekman, A.N. (2008). *A comparison of experimental ReMi measurments with various source,*
719 *array, and site condition*, (master's thesis). University of Arkansas.

720 Ben-Menahem, A., & Singh, S.J. (1981). *Seismic waves and sources*. New York: Springer-
721 Verlag.

722 Berti, M., Martina, M.L.V., Franceschini, S., Pignone, S., Simoni, A., & Pizziolo, M., (2012).
723 Probabilistic rainfall thresholds for landslide occurence using a Bayesian approach. *Journal of*
724 *Geophysical Research*, *117*, 1-20.

725 Bovis, M.J., & Jones, P. (1992). Holocene history of earth flow mass movement in South central
726 British Columbia: the influence of hydroclimatic changes. *Can. Journal Earth Sci., 29*, 1746-
727 1755.

728 BSI (2015). *BS 5930: 2015—The Code of Practice for Site Investigations*. British Standards
729 Institute, Milton Keynes.

730 Casagrande, A. (1932). Research on the Atterberg Limits of Soils. *Public Roads*, *13*(8), 121–136.

731 Castellaro S. (2016). Soil and structure damping from single station measurements. *Soil*
732 *Dynamics and Earthquake Engineering*, *90*, 480-493.

733 Coe, J.A., McKenna, J.P., Godt, J.W., & Baum, R.L (2009). Basal-topographic control of
734 stationary ponds on a continuously moving landslide. *Earth Surf. Process. Landf., 34*, 264-279.

735 Coussot, P., Laigle, D., Arattano, M., Deganutti, A., & Marchi, L. (1998). Direct Determination
736 of Rheological Characteristics of Debris Flow, *Journal of Hydraulic Engineering*, *124*(8), 865-
737 868.

738 Cox, B.R., & Wood, C.M. (2010). *A comparison of linear array surface wave methods at soft*
739 *soil site in the Mississippi Embayment*. Paper presented at GeoFlorida 2010, Orlando, Florida.

740 Craig, D. (1979). *Some apsects of mudslide stability in East County Antrim, Northern Ireland*,
741 (Doctoral thesis). Queen's University of Belfast, Ireland.

742 Cruden, D.M., & Varnes, D.J. (1996). Landslide types and processes. In: Turner, A.K. and
743 Shuster, R.L. (Eds.), *Landslides: Investigation and Mitigation*, (Special Report No. 247, 36-75),
744 Washington: National Academy Press.

745 D'Elia, B., Picarelli, L., & Leroueil, S. (1998). Geotechnical characterization of slope
746 movements in structurally complex clay soils and stiff jointed clays. *Rivista Italiana di*
747 *Geotecnica*, *33*, 5-32.

748 Foti, S., Lai G. C., Rix G. J., & Strobbia C. (2014). *Surface wave methods for near-surface site*
749 *characterization*. London: CRC Press.

750 Giordan, D., Allasia, P., Manconi, A., Baldo, M., Santangelo, M., Cardinali, M., Corazza, A.,
751 Albanese, V., Lollino, G., & Guzzetti, F. (2013). Morphological and kinematic evolution of a
752 large earthflow: The Montaguto landslide, Southern Italy. *Geomorphology*, *187*, 61-79.

753 Gucunski, N, & Woods, R.D. (1992). Numerical simulation of the SASW test. *Soil Dyn. Earthq.*
754 *Eng.*, *11*, 213–27.

755 Hadziioannou, C., Larose, E., Coutant, O., Roux, P., & Campillo, M. (2009). Stability of
756 monitoring weak changes in multiply scattering media with ambient noise correlation:
757 Laboratory experiments, *J. Acoust. Soc. Am.*, *125*(6), 3688–3695.

758 Handwerger, A. L., Roering, J.J., & Schmidt, D.A. (2013). Controls on the seasonal deformation
759 of slow-moving landslides. *Earth and Planetary Sciences Letters*, 377-378.

760 Hang, P. T., & Brindley G.W. (1970). Methylene blue absorption by clays minerals.
761 Determination of surface areas and cation exchange capacities (clay organic studies XVIII).
762 *Clays and clay minerals*, *18*(4), 203-212.

763 Hoek, E., & Brown, E.T. (1977). Practical estimates of rock mass strength. *International Journal*
764 *of Rock Mechanics and Mining Sciences*, *34*(8), 1165-1186.

765 Holtz, R.D. & Kovacs, W.D. (1981). *An Introduction to Geotechnical Engineering*. Civil
766 Engineering and Engineering Mechanics Series, New Jersey: Prentice-Hall.

767 Hungr, O., Evans, S.G., Bovis, M.J., & Hutchinson, J.N. (2001). A review of the classification of
768 landslides the flow type. *Environ. Eng. Geosci., 7*, 221–238.

769 Hutchinson, J.N. (1970). A coastal mudflow on the London clay cliffs at Beltinge, North Kent.
770 *Geotechnique*, *20*(4), 412-438.

771 Hutchinson, J.N. & Bhandari, R.K. (1971). Undrained loading, a fundamental mechanism of
772 mudflows and other mass movements. *Geotechnique*, *21*(4), 353-383.

773 Hutchinson, J. N., Prior, D. B., & Stephens, N. (1974). Potentially dangerous surges in an Antrim
774 [Ireland] mudslide: *Quarterly Journal of Engineering Geology*, *7*(4), 363-376.

775 Hutchinson, J.N. (1988). *General report: morphological and geotechnial parameters of*
776 *landslides in relation to geology and hydrogeology*. Paper presented at Fifth International
777 Symposium on Landslides, Rotterdam, Netherlands.

778 Iverson, R.M., & Major, J.J. (1987). Groundwater seepage vectors and potential for hillslope
779 failure and debris flow mobilization. *Water Resources Research*, *22*(11), 1543-1548.

780 Jones, R. (1962). Surface wave technique for measuring the elastic properties and thickness of
781 roads: Theoretical development. *British Journal of Applied Physics*, *13*(1), 21-29.

782 Jongmans, D., Baillet, L., Larose, E., Bottelin, P., Mainsant, G., Chambon, G., & Jaboyedoff M.
783 (2015). *Application of ambient vibration techniques for monitoring the triggering of rapid*
784 *landslides*. Paper presented at *Engineering Geology for Society and Territory*, Torino, Italy.

785 Keefer, D.K., & Johnson, A.M. (1983). *Earthflows: morphology, mobilization and movement*.
786 U.S. Geological Survey Professional Paper (1264), U.S. Government Printing Office.

787 Lautrin, D. (1989). Utilisation pratique des parametres derives de l'essai au blue de methylene
788 dans le les projets de genie civile. *Bulletin de Liaison des laboratories des ponts et Chaussees*,
789 *160*, 29-41.

790 Louie, J.N. (2001). Faster, better: shear-wave velocity to 100 meters depth from refraction
791 microtremor arrays. *Bulletin of Seismological Society of America*, *91*(2), 347-364.

792 Mainsant, G., Larose, E., Bronnima, C., Jongmans, D., Michoud, C., & Jaboyedoff, M. (2012a).
793 Ambient seismic noise monitoring of a clay landslide: toward failure prediction. *Geophisical*
794 *Research Letters*, *117*, 1-12. https://doi.org/10.1029/2011JF002159.

795 Mainsant, G., Jongmans, D., Chambon, G., Larose, E., & Baillet, L. (2012b). Shear-wave
796 velocity as an indicator for rheological changes in clay materials: Lessons from laboratory
797 experiments. *Geophysical Research Letters*, *39*(19), 1-5.

798 Mainsant, G., Chambon, G., Jongmans, D., Larose, E., & Baillet, L. (2015). Shear-wave-velocity
799 drop prior to clayey mass movement in laboratory flume experiment. *Engineering Geology*, *192*,
800 26-32.

801 Mayne, P., (2007). *Cone Penetration Testing, a synthesis of highway practice*. Washington D.C.:
802 Trasportation Research Board.

803 Moore, R. (1988). *The clay mineralogy, weathering and mudslide behaviour on coastal cliffs*,
804 (Doctoral thesis). King's College, University of London.

805 Mulargia F., & Castellaro S. (2013). A seismic passive imaging step beyond SPAC and
806 ReMiTM. *Geophysics*, *78*, 63-72.

807 Nguyen, H.Q., DeGroot D.J. & Lunne T. (2014). *Small strain shear modulus of marine clays*
808 *from CPT*. Paper presented at 3rd International Symposium on Cone Penetration Testing, Las
809 Vegas, Nevada, USA.

810 Ortiz,M., & Simo, J.S. (1986). An analysis of a newclass of integration algorithms for
811 elastoplastic constitutive relation. *Int. Jou. Numerical Methods in Engineering*, *23*(3), 353-366.

812 Park, C., Miller, R., & Xia, J. (1999). Multi-channel analysis of surface waves. *Geophysics*,
813 *64*(3), 800-808.

814 Park, C. B., Miller, R. D., Xia, J., & Ivanov, J. (2007). Multichannel analysis of surface waves
815 (MASW) —Active and passive methods. *The Leading Edge*, *26*(1), 60–64.

816 Pastor, M., Blanc, T., & Pastor, M.J. (2009). A depth integrated viscoplastic model for dilatant
817 saturated cohesive-frictional fluidized mixtures: Application to fast catastrophic landslides.
818 *Journal of non-Newtonian fluid mechanics*, *158*(1-3), 142-153.

819 Pastor, M., Manzanal, D., Fernandez Merodo, J.A., Mira, P., Blanc, T., Drempetic, V., Pastor,
820 M.J., Haddad, B., & Sanchez, M. (2010). From solids to fluidized soils: diffuse failure
821 mechanisms in geostructureswith applications to fast catastrophic landslides. *Granular Matter*,
822 *12*(3), 211-228.

823 Picarelli, L., Urcioli, L., Ramondini, G., & Comegna, L. (2005). Main features of mudslides in
824 tectonised highly fissured clays shales. *Landslides*, *2*(1), 15-30.

825 Prior, D.B., Stephens, N., & Archer, D.R. (1968). Composite mudflows on the Antrim coast of
826 north east Ireland. *Geografiska Annaler*, *50*(A), 65-78.

827 Reynolds, J.M. (1997). *An introduction to applied and environmental geophysics*. Chichester:
828 John Wiley.

829 Ricci Lucchi, F., Bassetti, M.A., Manzi, V., & Roveri, M. (2002). Il Messiniano trent'anni dopo:
830 eventi connessi alla crisi di salinità dell'avanfossa appenninica. *Studi Geol. Camerti*, *1*, 127-142.

831 Richart, F. E., Hall, J. R., & Woods, R. D. (1970). *Vibrations of soils and foundations*.
832 Englewood Cliffs, NJ: Prentice-Hall, Inc.

833 Rix, G. J., & Leipski, E.A. (1991). Accuracy and resolution of surface wave inversion. In:
834 Bhatia, S. K., and Blaney, G. W. (Eds.), *Recent advances in instrumentation, data acquisition*
835 *and testing in soil dynamics,* Am. Soc. Civil Eng., San Diego, CA.

836 Robertson, P.K. (2009). Evaluation of flow liquefaction and liquefied strengh using the cone
837 penetration test. *Journal of Geotechnical and Geoenvironmental Engineering*, *136*(6), 842-853.

838 Robertson, P.K. (2010). *Estimating in situ state parameter and friction angle in sandy soils from*
839 *CPT*. Paper presented at 2nd Internation Symposium of Cone Penetration Test, Signal Hill,
840 California, USA.

841 Santos, J.A, & Correia, G. (2000). *Shear modulus of soils under cyclic loading at small and*
842 *medium strain level*. Paper presented at 12WCEE 2000, Auckland, New Zeland.

843 Schadler, W. (2010). *Slope movements of the earthflow type - engineering -geological*
844 *investigation, geotechnical assessment, and modelling of the source areas on the basis of case*
845 *studies from the Alps and Apennines*. Berlin: Logos verlag Berling GmbH.

846 Schulz, W. H., Mackenna, J. P., Kibler, J. D., & Biavati, G. (2009). Relations between hydrology
847 and velocity of a continuously moving landslide – evidence of pore pressure feedback regulating
848 landslide motion? *Landslides*, *6*, 181-190.

849 Seed R.B., Cetin K.O., Moss. R.E.S., Kammerer, A.M., Wu, J., Pestana, J.M., Riemer, M.F.,
850 Sancio R.B., Bray J.D., Kayen R.E., & Faris, A. (2003). *Recent advances in soil liquefaction*
851 *engineering: a unified and consisted framework*. Eartquake Engineerig Research Center, Report
852 No. EERC 2003-6, California, USA.

853 Simoni, A., Ponza, A., Picotti, V., Berti, M., & Dinelli, E. (2013). Earthflow sediment
854 production and Holocene sediment record in a large apenninic catchment. *Geomorphology*, *188*,
855 42-53.

856 Starr, J.L. & Paltineanu, I.C. (2002). Methods for measurement of soil water content:
857 Capacitance devices. In: Dane J.H., Topp G.C., (Eds), *Methods of Soil Analysis: Part 4 Physical*
858 *Methods*. Madison, WI: Soil Science Society of America.

859 Strobbia, C., & Cassiani, G. (2011). Refraction microtremors: Data analysis and diagnostics of
860 key hypotheses. *Geophysics*, *76*(3), MA11-MA20.

861 Telford M.W., Geldart, L. P., & Sheriff, E.R. (1990). *Applied geophysics*. Cambridge:
862 Cambridge University Press.

863 Terzaghi, K. (1925). *Erdbaumechanik auf Bodenphysikalischer Grundlage*. Franz Deuticke,
864 Liepzig-Vienna.

865 Terzaghi, K.,(1943). *Theoretical Soil Mechanic*. New York : John Wiley and Sons.

866 Tokimatsu, K., Tamura, S., Kojima, H. (1992). Effects of multiple modes on Rayleigh wave
867 dispersion characteristics. *Journal Geotech. Eng.*, *118*, 1529–43.

868 Tokimatsu, K. (1997). *Geotechnical site characterization using surface waves*. Paper presented
869 at 1st Intl. Conf. Earthquake Geotechnical Engineering, Tokyo.

870 Van Asch, T. W. J., & Malet, J.P. (2009). Flow-type failures in fine-grained soils: an important
871 aspect in landslide hazard analysis. *Nat. Hazards Earth Syst. Sci., 9*(5), 1703–1711.

872   Varnes, D.J. & Savage, W.Z. (1996). *The Slumgullion earth flow: a large scale natural*
873   *laboratory*. U.S Geological survey bulletin (2130), U.S. Government Printing Office.

874 **Figure Captions**

875 Figure 1. Geological map of the study area. The capital letters (A, B and C) indicate the source
876 areas of the Montevecchio earthflow. The red line shows the boundary of the landslide in July
877 2015. The colored dotted lines show the three reactivations and the evolution of the headwall
878 scarp in source areas A and B.

879 Figure 2. Photographs of the Montevecchio earthflow in July 2015. a) panoramic view of the
880 source area A with the upper part of the earthflow channel; b) main reach of the earthflow
881 channel; c-d) deposition area after the second reactivation of February 2015.

882 Figure 3. Conceptual example of the MASW/ReMi analysis. Top left: schematic geophone array
883 (G1-G6). Top right: flowchart of the solving algorithm. Bottom: frequency-velocity plot showing
884 the experimental propagation velocity distribution of a surface wave at a specific frequency. The
885 graduated colour bar shows the probability density distribution of the normalized cross-
886 correlation function; the blue dots indicate the most probable velocity values for each frequency.
887 The point A indicates the Rayleigh velocity for a frequency of 30 Hz and the associated error
888 bar, defined as the velocity range with a probability value higher than 0.8.

889 Figure 4. Map showing the location of the monitoring system and periodic seismic surveys.

890 Figure 5. Photographs showing the difficult ground conditions encountered during periodic
891 seismic surveys. a-b) cracks and open fractures characterize the landslide surface during the dry
892 period; c) water ponds and soft soil reduce the accessibility soon after a reactivation or an intense
893 rainfall.

894 Figure 6. Rayleigh-wave phase-velocity spectra acquired on January 23 2015 along section C
895 (a=active survey; b=passive survey). Numbers 1 to 8 indicate the geophones.

896 Figure 7. Photographs of the Montevecchio monitoring system. a) geophone amplifiers inserted
897 in a plastic box; b) continuous monitoring system installed in the main track of the earthflow
898 channel. c-d) equipment damaged by a reactivation of the earthflow.

899 Figure 8. Example of three dispersion curves acquired by the monitoring system. These curves
900 were classified as 'good' (a), 'fair' (b), and 'bad' (c) according to the quality of the phase
901 velocity spectrum (see text). Numbers 1 to 8 indicate the geophones. The graduated colour bars
902 show the probability density distribution of the normalized cross-correlation function.

903 Figure 9. Rayleigh wave velocity profiles measured after the reactivation of April 27, 2014
904 inside (A, B, C, D) and outside (E, F) the landslide. Note the change in scale between A-D and
905 E-F. Locations of each site are shown in Figure 4.

906 Figure 10. Rayleigh wave velocity profiles measured after the reactivation of February 25, 2015
907 inside (B, C, D) and outside (E) the landslide. Note the change in scale for site E. Sites F and G
908 (located outside the landslide) are not shown because the Rayleigh velocity profiles remained
909 constant. Locations of each site are shown in Figure 4.

910   Figure 11. Rayleigh wave velocity profiles measured in the period June 2015-September 2015
911   inside the landslide. Sites F and G (located outside the landslide) are not shown because the
912   Rayleigh velocity profiles remained constant. Locations of each site are shown in Figure 4.

913   Figure 12. Variation of Rayleigh wave velocity with time during the whole period of
914   measurement. Each point indicates the value measured at a depth of 2 m. Arrows show the start
915   of the main reactivation events of the earthflow.

916   Figure 13. Comparison between (a) rainfall and cumulative displacement, (b) displacement rate
917   and (c) Rayleigh velocity measured by the monitoring system before and after the reactivation of
918   May 25, 2015.

919   Figure 14. Comparison between (a) rainfall and cumulative displacement, (b) displacement rate
920   and (c) Rayleigh velocity measured by the monitoring system from June to August 2015.

921   Figure 15. Comparison between (a) rainfall and cumulative displacement, (b) displacement rate
922   and (c) Rayleigh velocity measured by the monitoring system before the reactivation of February
923   25, 2015.

924   Figure 16. Comparison between (a) rainfall and cumulative displacement, (b) displacement rate
925   and (c) Rayleigh velocity measured by the monitoring system during the suspended phase from
926   July to November 2014.

927   Figure 17. Charts showing the variation of Rayleigh velocity at a depth of 2 m (a) and the
928   corresponding variation of small-strain shear stiffness (b) with the time elapsed after a surge.
929   Each point represents the mean value of V_r or G_0 obtained by periodic surveys inside (gray dots)
930   or outside (black triangles) the landslide area.

931   Figure 18. Variation of the normalized void ratio (see text) with the time elapsed after a surge.
932   Each point represents the mean value of void ratio obtained by periodic surveys inside the
933   landslide area. Red lines indicate the theoretical trend predicted by the one-dimensional Terzaghi
934   equation for two values of the coefficient of consolidation c_v typical of fine-grained materials.
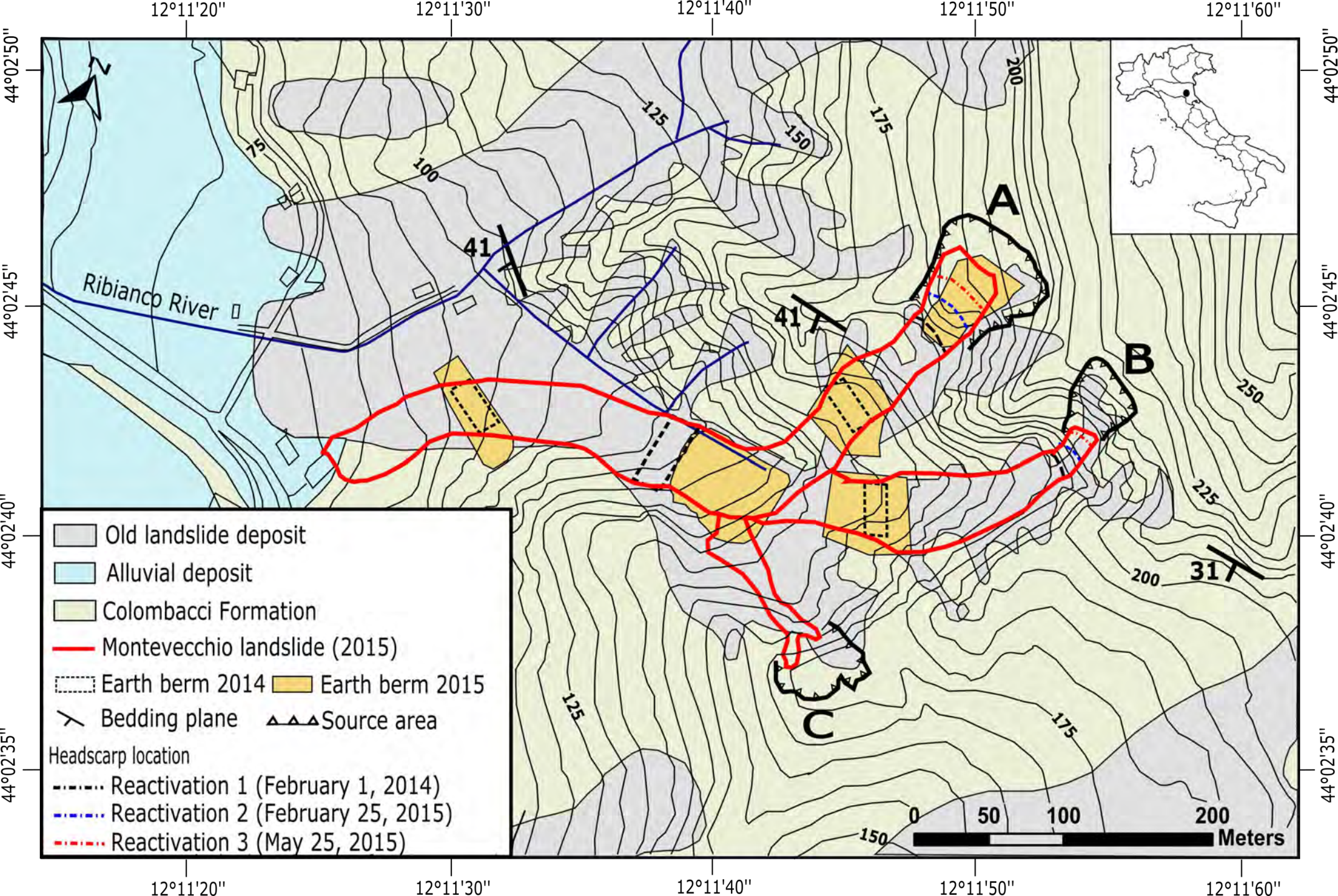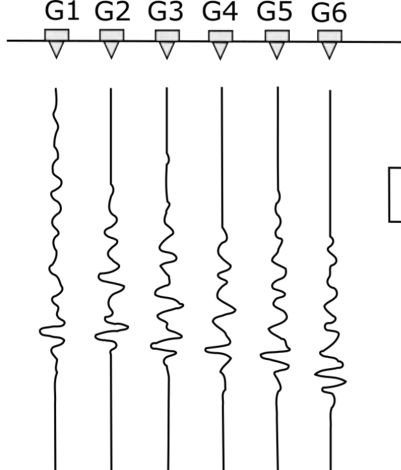
935

Figure 1.

Legend:

- Old landslide deposit
- Alluvial deposit
- Colombacci Formation
- Montevecchio landslide (2015)
- Earth berm 2014
- Earth berm 2015
- Bedding plane
- Source area

Headscarp location
- Reactivation 1 (February 1, 2014)
- Reactivation 2 (February 25, 2015)
- Reactivation 3 (May 25, 2015)

Ribianco River

0   50   100   200
Meters
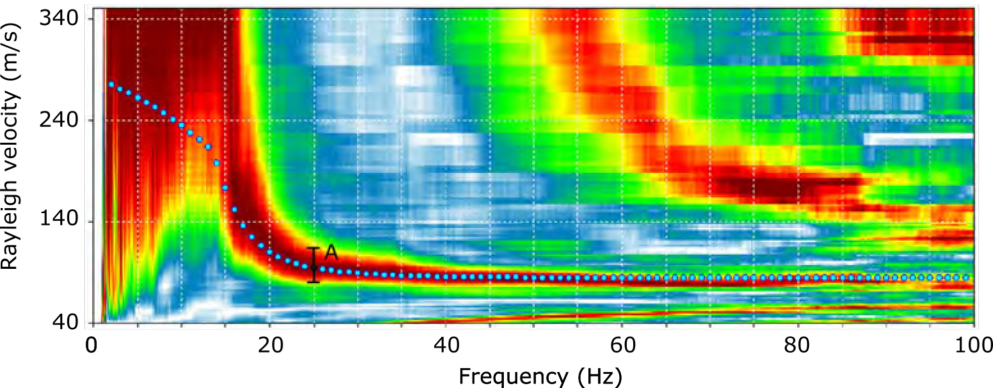
Figure 2.
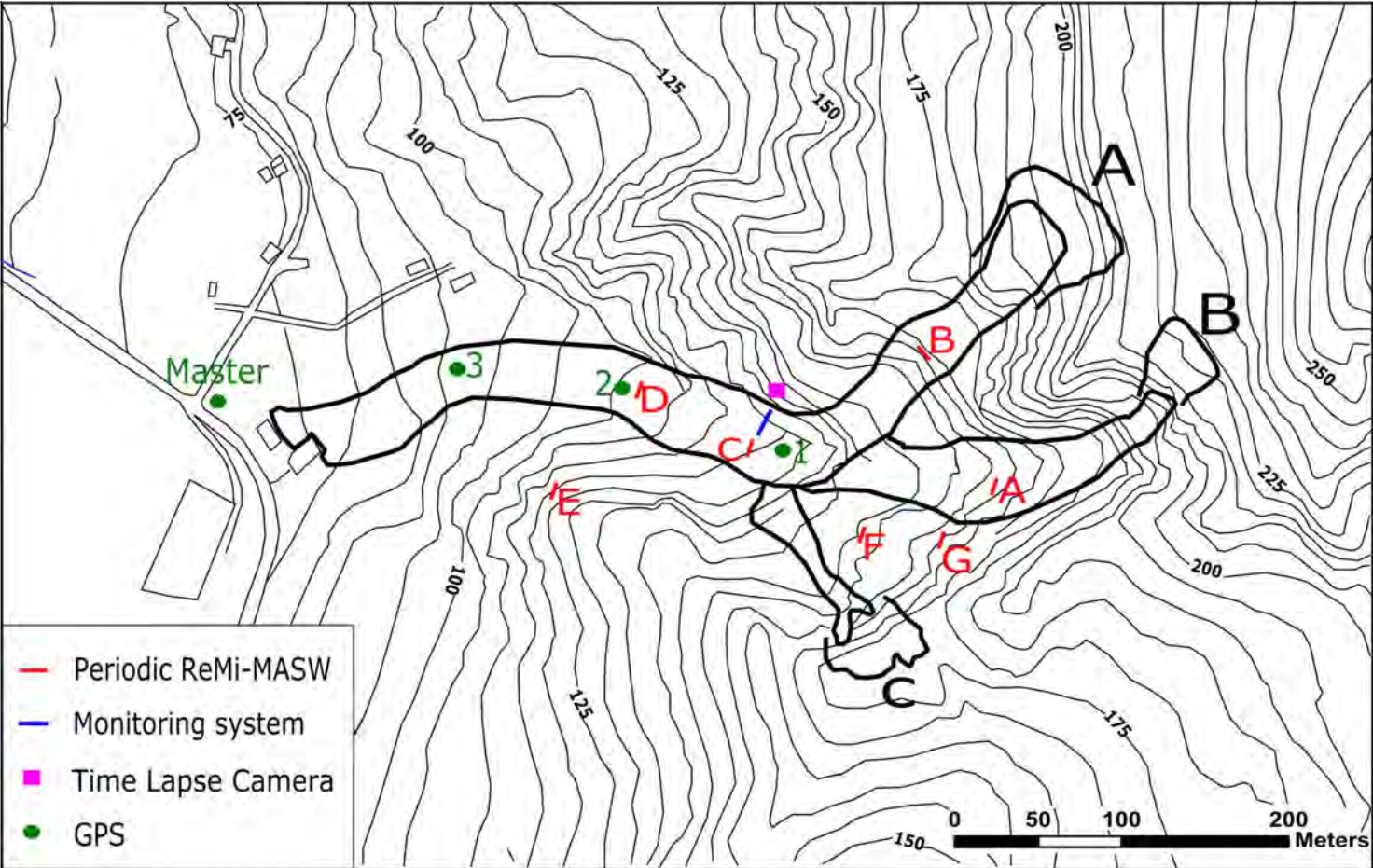
Figure 3.

Figure 4.

Figure 5.

Figure 6..

Figure 7.

a
b
c
d

Figure 8.

Figure 9.

Days after the reactivation of April 27, 2014
- 10
- 38
- 93
- 123
- 271

Figure 10.

B

C

D

E

14
27
51
58
64
71

Days after the reactivation
of February 25, 2015

--- Data of the first period

Figure 11.

Legend (panel A):
14
25
45
52
72
94
102
Days after the reactivation of May 25, 2015

Figure 12.

1A) Reactivation of February 1, 2014
1B) Reactivation of April 27, 2014
2) Reactivation of February 25, 2015
3) Reactivation of May 25, 2015

Inside the landslide
▲ A   ◆ B
● C   ■ D

Outside the landslide
▲ E   ● F   ■ G
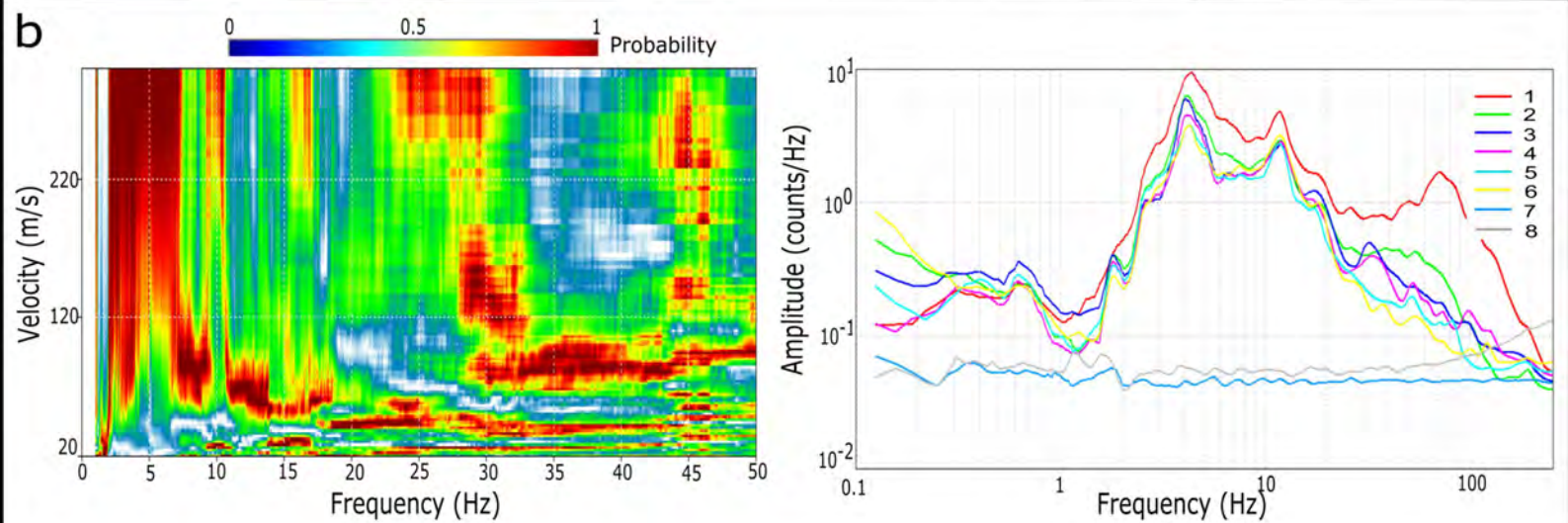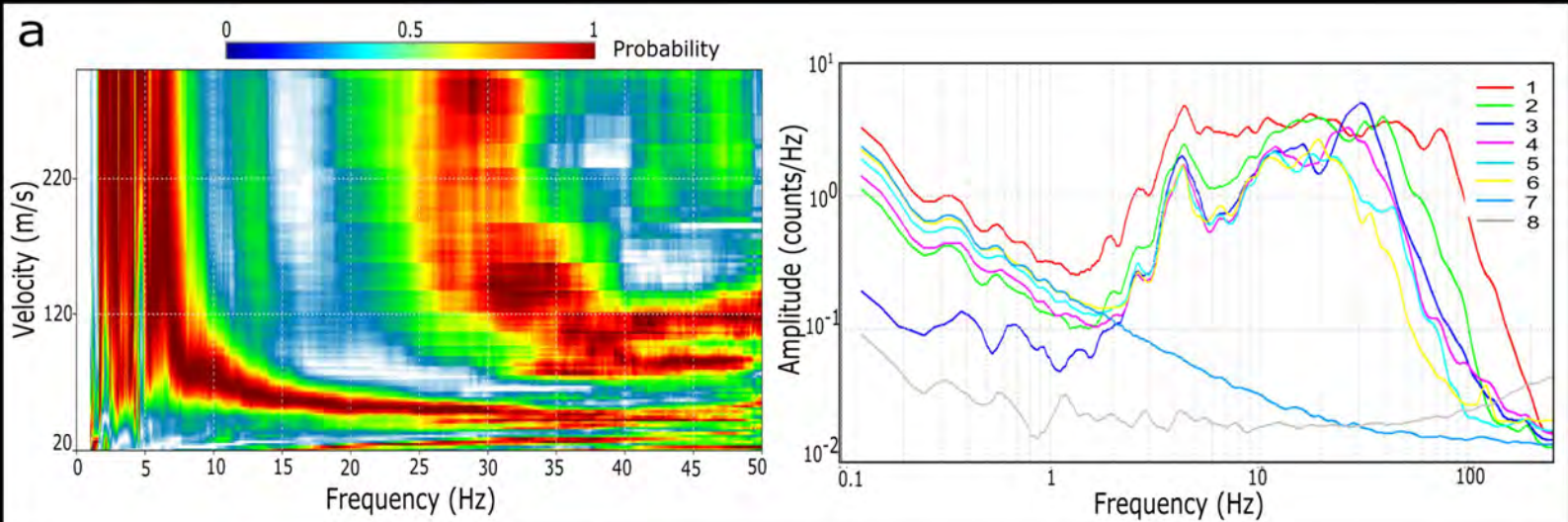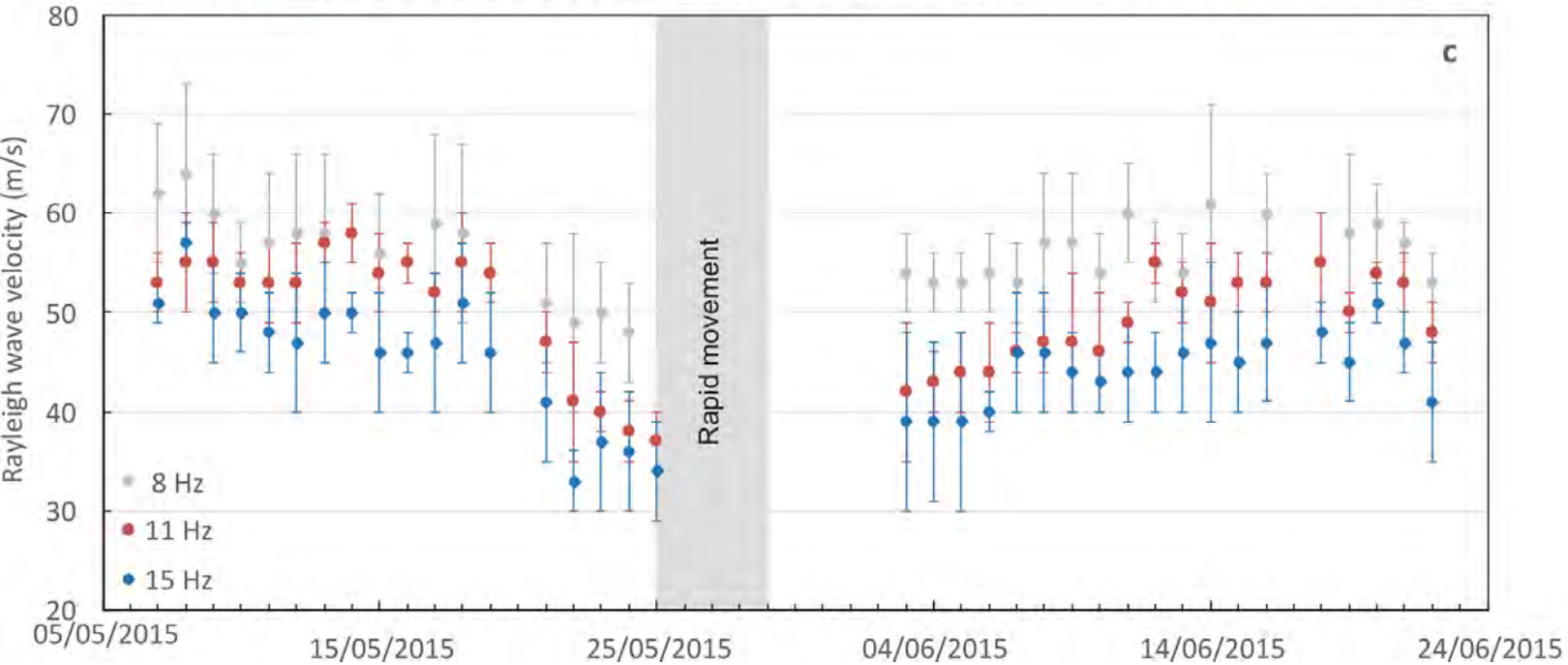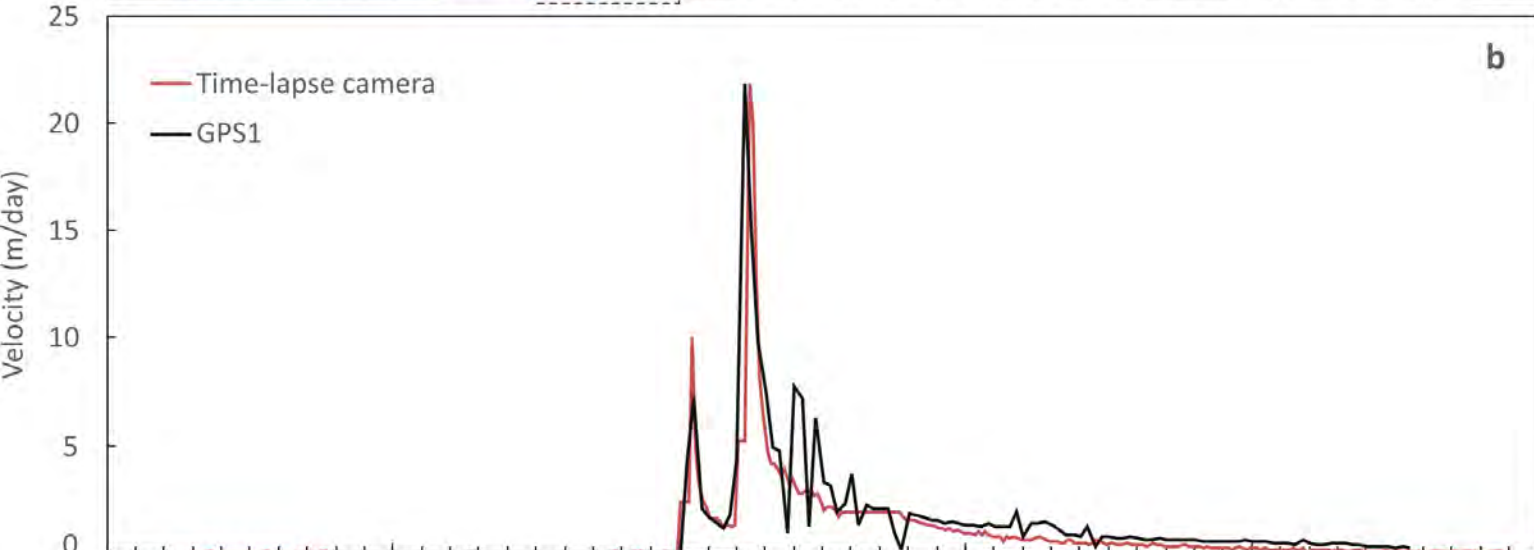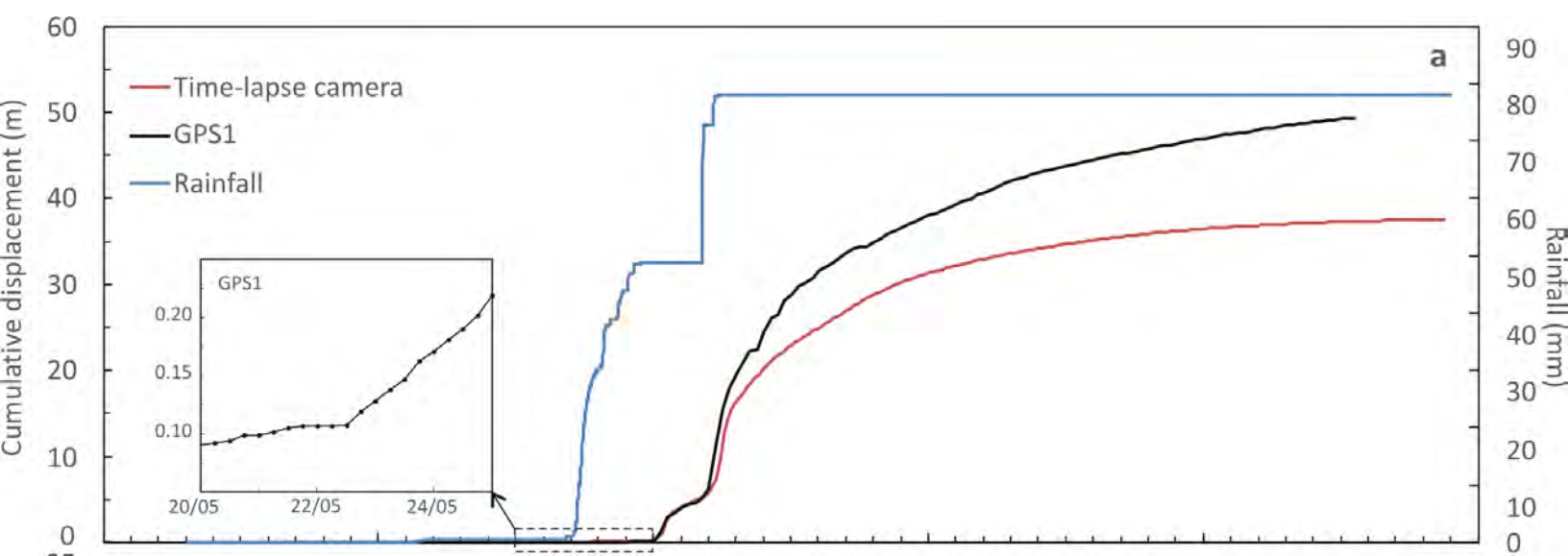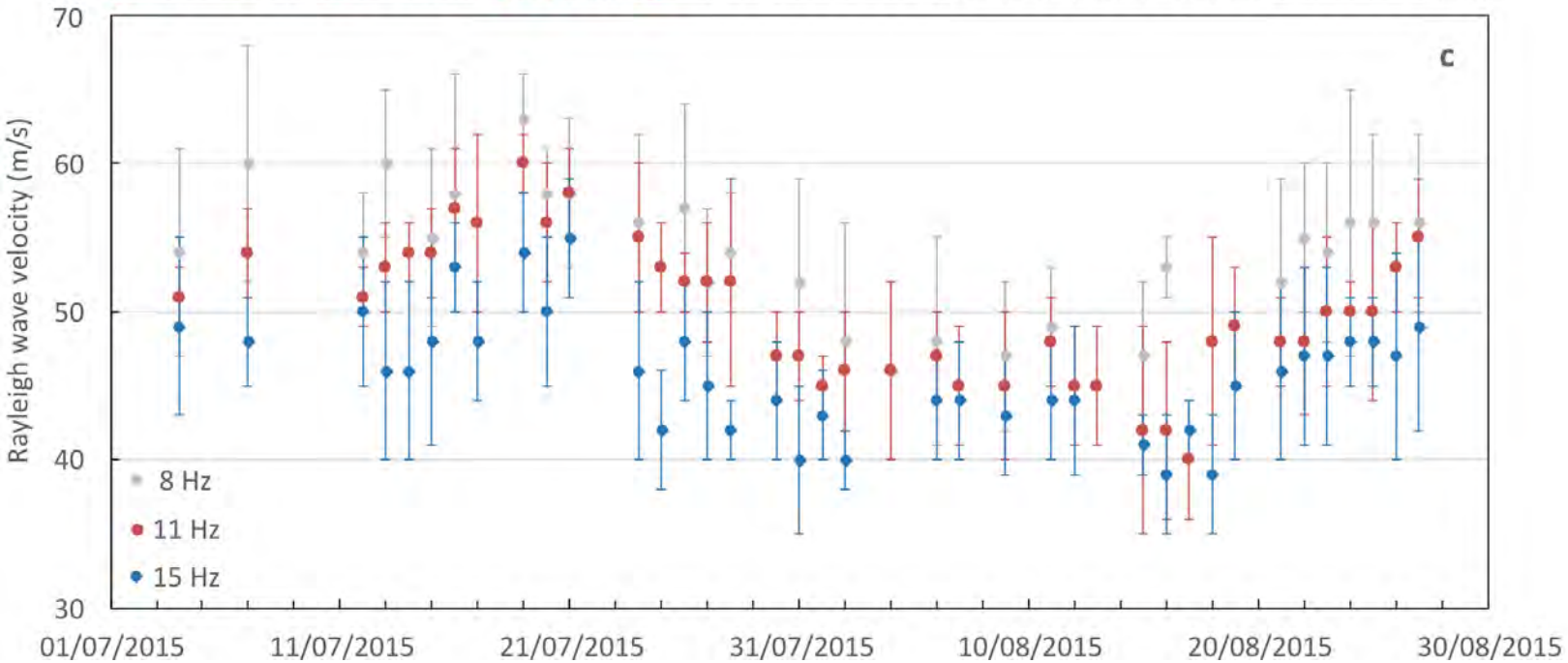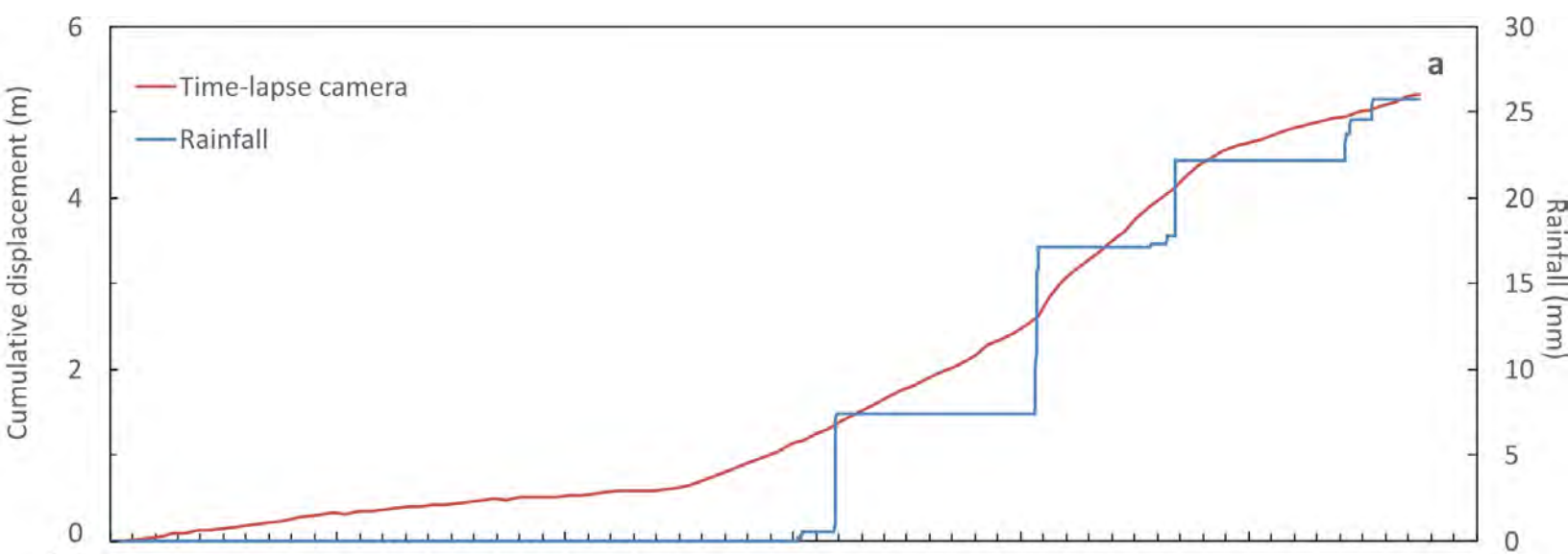
Figure 13.

Figure 14.

Figure 15.

Figure 16.

Figure 17.

$V_r = 50 \cdot t^{0.13}$

Legend:
- ○ Inside the landslide
- ▲ Outside the landslide

Panel a: Surface wave velocity, V_r (m/s) vs Time after failure, t (days)

Panel b: Small-strain shear modulus, G_0 (MPa) vs Time after failure, t (days)

Figure 18.